PNAS RESEARCH ARTICLE | NEUROSCIENCE

Anterior and posterior retrosplenial cortex employ distinct strategies for egocentric–allocentric transformation in spatial coding

Youran Yang[a,b,c], Xiang Zhang[a,b], Xin Yuan[a,b,c], Haiqian Cai[a,b,d], Qichen Cao[a,b,c], and Chenglin Miao[a,b,c,d,e,f,1]

Affiliations are included on p. 11.

Edited by György Buzsaki, New York University Grossman School of Medicine, New York, NY; received January 8, 2026; accepted June 24, 2026

The transformation from egocentric to allocentric spatial coordinates is a critical process in neural spatial computation. The retrosplenial cortex (RSC) is hypothesized to serve as a central hub for this conversion, bridging egocentric perceptual inputs with allocentric representations in hippocampal and parahippocampal circuits. However, the regional and projection-specific organization of this function within the RSC remains poorly defined. In this study, we employed two-photon calcium imaging in freely navigating mice to dissect RSC spatial coding. We identified functional differences along the anteroposterior axis: the anterior RSC (aRSC) was predominantly characterized by egocentric boundary vector (EBV) coding, whereas the posterior RSC (pRSC) exhibited enhanced allocentric boundary representation. And it reveals that egocentric boundary vector cells (EBVCs) in the pRSC possess broader egocentric tuning than those in the aRSC. Despite this, pRSC shows tighter integration of allocentric head direction information, which converges specifically onto specialized conjunctive cells, resulting in a more selective boundary representation. Crucially, this work identifies functional differences along the RSC, where spatial coding transforms from more egocentric in aRSC to more allocentric in pRSC. Furthermore, it defines a specialized RSC to medial entorhinal cortex (MEC) projection pathway that is enriched for these global-tuned, conjunctive neurons, providing the MEC with a highly integrated, world-referenced spatial signal for constructing cognitive maps. Our findings elucidate a functional variance and projection-specific circuitry within the RSC, providing experimental evidence for models of hierarchical spatial processing.

retrosplenial cortex | spatial navigation | egocentric and allocentric coding | neural circuits

Significance

This study reveals a functional variance in the retrosplenial cortex (RSC) for spatial processing. Using calcium imaging in mice, researchers found the anterior RSC (aRSC) predominantly encodes egocentric boundary vectors. In contrast, the posterior RSC (pRSC) integrates this egocentric information with head-direction to create sharpened allocentric boundary representations. Crucially, the function of a specific neuronal subpopulation projecting to the medial entorhinal cortex (RSC→MEC) was identified. These cells form more abstract, global allocentric representations, enriching spatial information for downstream navigation circuits. This refines hierarchical spatial processing models, highlighting subregion- and projection-specific computations within the RSC.

The mammalian brain constructs spatial maps through a hierarchical system, progressing from sensory-driven, egocentric encoding of local cues in parietal areas to abstract, allocentric cognitive maps in the hippocampus (1–4). A central computational challenge in this process is building a stable, world-centered (allocentric) map from transient, self-centered (egocentric) sensory inputs. The retrosplenial cortex (RSC), positioned at a pivotal point within this hierarchy, is strongly implicated as a critical hub for transforming egocentric information into an allocentric reference frame (5–7), given its dense bidirectional connectivity with both egocentric and allocentric processing centers (5, 8, 9). Supporting this, RSC lesions impair navigation requiring either allocentric (10) or egocentric (11) strategies, underscoring its role in integrating diverse spatial features to guide behavior. A primary theoretical bridge for this transformation involves egocentric boundary vector cells (EBVCs), which are thought to encode a real-time, egocentric vector map of distances to environmental boundaries (12, 13). By integrating this information with self-motion cues, the brain can infer stable, allocentric boundary positions, forming a foundational scaffold that anchors hippocampal place fields and calibrates entorhinal grid cell metrics (14, 15). However, how the RSC specifically contributes to this process along its anterior–posterior axis remains unclear.

Anatomical evidence suggests a potential anterior–posterior gradient of functional specialization within the RSC (16–20). While projections from spatially modulated structures show topographic organization along the RSC A-P axis, the functional implications of this organization remain unclear.

A major output target of the posterior RSC (pRSC) is the medial entorhinal cortex (MEC), a key site for spatial computation where grid cells, border cells, and head direction cells collectively encode environmental geometry and self-motion (21–25). Anatomical tracing studies confirm topographically organized projections from the posterolateral RSC to the MEC (16, 18, 26–32). Despite this, the functional logic of these RSC→MEC projections is unclear. Critical questions persist: Do RSC subregions differentially process boundary-related signals? How is this information selectively routed to MEC microcircuits? Specifically, it is unknown

Author contributions: Y.Y., Q.C., and C.M. designed research; Y.Y. and H.C. performed research; Y.Y., X.Z., and X.Y. analyzed data; and Y.Y. and C.M. wrote the paper.

The authors declare no competing interest.

This article is a PNAS Direct Submission.

Copyright © 2026 the Author(s). Published by PNAS. This article is distributed under Creative Commons Attribution-NonCommercial-NoDerivatives License 4.0 (CC BY-NC-ND).

[1]To whom correspondence may be addressed. Email: chenglin.miao@pku.edu.cn.

This article contains supporting information online at https://www.pnas.org/lookup/suppl/doi:10.1073/pnas.2600565123/-/DCSupplemental.

Published July 28, 2026.

Downloaded from https://www.pnas.org by PEKING UNIVERSITY on August 3, 2026 from IP address 222.29.65.227.

whether RSC→MEC projection neurons simply relay spatial signals or actively transform information through local integration. Resolving these questions is fundamental to understanding how the RSC-MEC network supports dynamic spatial representations during navigation.

To address these gaps, we combined two-photon imaging in freely behaving mice with projection-specific functional analysis. Using generalized linear model (GLM), we systematically quantified the prevalence of EBVCs and conjunctive coding [e.g., head direction (HD) × boundary tuning] across the anterior and posterior RSC. This approach allowed us to investigate spatial transformation of egocentric boundary and allocentric head-direction encoding. Furthermore, we compared RSC→MEC projecting neurons with the general RSC population to elucidate functional segregation along the anteroposterior axis and characterize the nature of spatial information transmitted to the MEC.

Results

EBVCs in pRSC Exhibit Distinct Egocentric Tuning Properties Compared to aRSC. Given the distinct anatomical inputs to anterior RSC (aRSC) and pRSC, we hypothesized they would exhibit differential spatial coding properties. We specifically targeted the posterolateral pRSC subregion which projects to the MEC and compared it to aRSC using microendoscopic calcium imaging in mice navigating an open-field arena (Fig. 1 *A–C* and *SI Appendix*, Fig. S1 *A* and *B*).

We identified multiple functional cell types related to spatial navigation in both subregions, including EBVCs (12), angular head velocity cells (AHVCs) (33), place cells (PCs), and speed cells (SCs) (33) (Fig. 1 *D–K* and *SI Appendix*, Fig. S2 *A–F*). The most pronounced difference between subregions was observed in EBVCs. Compared to aRSC, pRSC EBVCs displayed significantly broader egocentric tuning, evidenced by a reduced mean resultant length (MRL) (Fig. 1 *D* and *E*). pRSC EBVCs also showed smaller receptive field sizes (Fig. 1*E*), but did not differ in the distribution of their firing fields (*SI Appendix*, Fig. S2 *G–I*).

Due to the large imaging field, it is unable to precisely assign laminar identities to each region within every field of view. Therefore, we do not demonstrate laminar-specific functional distribution in this work.

pRSC Exhibits Enhanced Population-Level Conjunctive Coding Despite Fewer Functional Neurons. Having established a difference in egocentric tuning at the single-cell level, we next asked whether this extends to population-level coding strategies. We investigated allocentric boundary coding by identifying boundary distance cells (BDCs), which fire at specific distances from environmental boundaries. The aRSC showed significantly higher proportions of PCs and BDCs (Fig. 1*L*). Although the pRSC contained a lower overall proportion of functionally tuned neurons compared to the aRSC (*SI Appendix*, Fig. S2*J*), and the percentages of all 15 possible pairwise conjunctive coding cell types were correspondingly reduced in the total population (Fig. 1*M*), pRSC demonstrated higher overlap index and more conjunction types with observed cell counts significantly exceeding expected values (*SI Appendix*, Fig. S2*K*). This finding suggests that though pRSC encodes spatial coding more sparsely, it integrates information across different modalities within its neuronal population.

pRSC Displays Enhanced Selectivity for Allocentric Boundary Identity. The observed conjunctivity in pRSC prompted us to investigate its functional consequence. We focused on BDCs and found that while the spatial information and peak firing locations of BDCs were similar between aRSC and pRSC (Fig. 2 *A–D*), the posterior region had a significantly lower proportion of BDCs (Fig. 1*L*). This resulted in a significantly higher decoding error for boundary distance in the posterior group (Fig. 2*E*).

To further dissect their functional profiles, BDCs were classified into BDCnear and BDCfar subgroups, to make the subsequent selectivity analysis more representative. These subgroups showed comparable spatial information at the population level between aRSC and pRSC (Fig. 2*F* and *SI Appendix*, Fig. S3 *A–C*). Interestingly, the posterior BDCnear population exhibited a significantly higher selectivity index than its anterior counterpart, indicating that pRSC encodes more specific information about boundary identity (Fig. 2 *G–I* and *SI Appendix*, Fig. S3*D*).

Allocentric Head Direction Information Is More Converged on EBVCs in Posterior than in aRSC. We next sought to determine how pRSC achieves this coding specificity. We found that the key lies not in the general HD cell (HDC) population, but in a specialized subset: the EBVC×HDC conjunctive cells. We hypothesized that the enhanced boundary selectivity in pRSC could result from a greater integration of allocentric HD information into its boundary coding. A conceptual model suggests that an EBVC tuned to a specific egocentric boundary will only fire when the animal faces a direction that brings that boundary into its receptive field, creating an allocentric, boundary-selective response (9) (Fig. 3*A*). We indeed found EBVC×HDC conjunctive cells in both regions that exhibited such boundary-selective firing (Fig. 3*B* and *SI Appendix*, Fig. S4*A*).

To test this hypothesis quantitatively, we used a GLM to dissect the contribution of allocentric HD (allo HD), egocentric boundary (ego), allocentric position (allo loc), and speed inputs to neuronal firing (Fig. 3*C*). Excluding allo HD inputs had a more detrimental effect on the model's performance for pRSC EBVCs, while excluding ego inputs had a greater impact on aRSC EBVCs (Fig. 3*D*).

At total population level, this differential input reliance revealed a clear anterior–posterior dichotomy with greater allo HD input influence in anterior total population than in posterior total population (Fig. 3*E*). Consistent with these observations, the anterior population demonstrated significantly stronger modulation by both allo pos and ego inputs compared to the posterior population, but there are no significant differences between aRSC and pRSC neurons' firing prediction when speed predictor excluded (*SI Appendix*, Fig. S4*B*).

Though the performance of the pRSC total population dropped less than that of aRSC when allo HD input was excluded, EBVC subpopulations showed no interregional differences in their dependence on allo HD signals. This indicates that while overall allo HD coding is effectively diluted posteriorly, EBVCs retain their coding capabilities, enabling a local integration where allo HD information is concentrated more effectively onto posterior EBVCs rather than being separated into distinct cell populations (Fig. 3*F*). As for other spatial information types, EBVCs showed no preferential encoding (*SI Appendix*, Fig. S4*C*). Further analysis revealed subregion-specific integration strategies: anterior EBVCs depended significantly less on allo HD inputs compared to local non-EBVCs (Fig. 3*G*), whereas posterior EBVCs and non-EBVCs exhibited comparable dependence (Fig. 3*H*). This contrast clarifies that although EBVCs across regions are similarly dependent on allo HD signals, the pRSC network integrates this information differently, effectively converging allo HD information onto EBVCs. At the single-cell level, the posterior EBVC population exhibited a significantly stronger bias toward relying on allo HD information (*SI Appendix*, Fig. S4 *D* and *E*).

Downloaded from https://www.pnas.org by PEKING UNIVERSITY on August 3, 2026 from IP address 222.29.65.227.

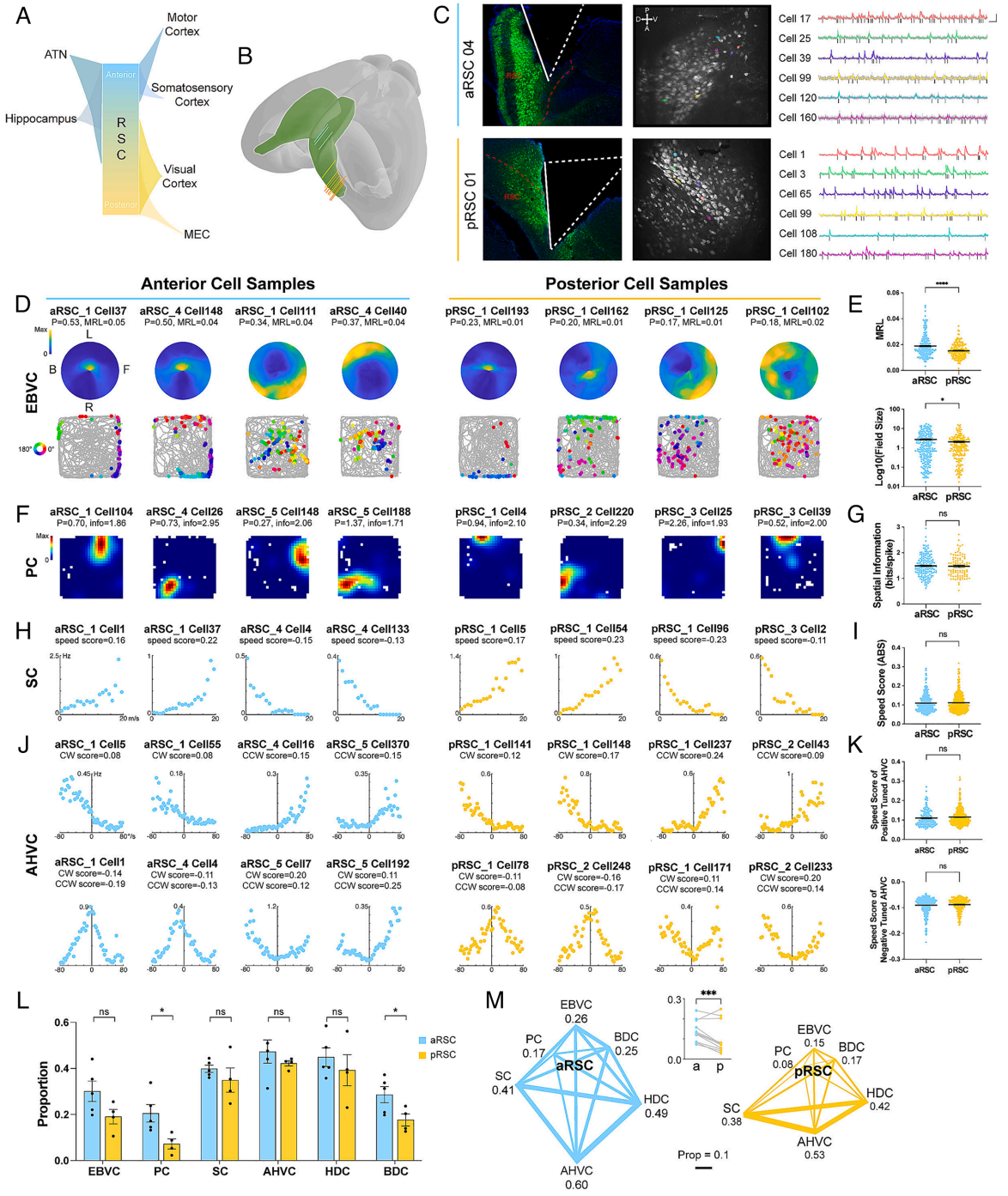


Fig. 1. Spatial related cell type population among anterior–posterior RSC. (*A*) The projection frame of the circuitry inputs of RSC. Adapted from https://brain-map.org. (*B*) Imaging sites in anterior and posterior part of RSC. *Left*: The green region represents the range of RSC. Each line represents a specific position of a sagittal imaging plane in RSC in an individual mouse. Blue: The sites of anterior total population imaging (N = 3, n = 920). Yellow: The sites of posterior total population imaging (N = 3, n = 1,263). Orange: The sites of RSC→MEC subpopulation imaging (posterior location) (N = 6, n = 534). (*C*) Recording example of anterior and posterior RSC imaging. *Left*: Post hoc histology validation of the imaging sample. (Scale bar, 200 mm.). *Middle*: Field of view (FOV) of the sample. (Scale bar, 100 μm.) *Right*: Calcium trace of sample cells recorded in the FOV. Gray trace: raw ΔF/F. Colored trace: denoised ΔF/F. Vertical lines below: deconvolved calcium events. Vertical Scale bar, dF/F = 2. Horizontal Scale bar, t = 10 s. (*D*) EBVC samples in anterior and posterior RSC. Upper: The ratemap in egocentric coordinate. Lower: The firing events plot colored by the corresponding head direction. Gray trace represents the trajectory of the mouse in the session. *Inset*: reference color of head direction. P: peak rate, F: front, B: behind, L: left, R: right. (*E*) The comparisons of the properties of EBVC between anterior and posterior RSC (aRSC n = 236, pRSC n = 184). *Upper*: MRL of EBVCs (Welch's *t* test, $P < 0.0001$). *Lower*: Logarithmic field size in egocentric ratemap of EBVCs (Welch's *t* test, $P = 0.0188$). (*F*) PC samples in anterior and posterior RSC showed by the ratemap. Info: spatial information. (*G*) Spatial information of PC in anterior and posterior RSC (Welch's *t* test, $P = 0.1702$; aRSC n = 156, pRSC n = 97). (*H*) SC samples in anterior and posterior RSC showed by the speed tuning curve. (*I*) Speed score of SC in anterior and posterior RSC (Welch's *t* test, $P = 0.4436$; aRSC n = 378, pRSC n = 486). (*J*) AHVC samples in anterior and posterior RSC showed by the speed tuning curve. *Upper* shows unidirectional AHVC samples, while *Lower* shows bidirectional AHVC samples. CW: clock-wise; CCW: counterclockwise. (*K*) Speed score of positive tuned AHVC (*Upper*, Welch's *t* test, $P = 0.1884$; aRSC n = 167, pRSC n = 440) and negative tuned AHVC (*Lower*, Welch's *t* test, $P = 0.3366$; aRSC n = 383, pRSC n = 231) in anterior and posterior RSC. (*L*) The proportion of functional cell types mentioned in this project in each recording of anterior (N = 5) or posterior (N = 4) RSC (Welch's *t* test, EBVC: $P = 0.0844$; PC: $P = 0.0222$; SC: $P = 0.4275$; AHVC: $P = 0.3746$; HDC: $P = 0.5408$; BDC: $P = 0.0411$). (*M*) The overall proportion of two-type conjunctive coding. The width of the line represents the proportion of the conjunctive cells in total population. The distance from the center to each cell types represents the proportion of the specific cell type in all population (the proportion is shown in number below the cell type names). *Inset*: proportion of the two-type conjunctive coding cell types in anterior and posterior RSC, corresponding to the line width in the hexagon (paired *t* test, $P = 0.0004$).

Downloaded from https://www.pnas.org by PEKING UNIVERSITY on August 3, 2026 from IP address 222.29.65.227.

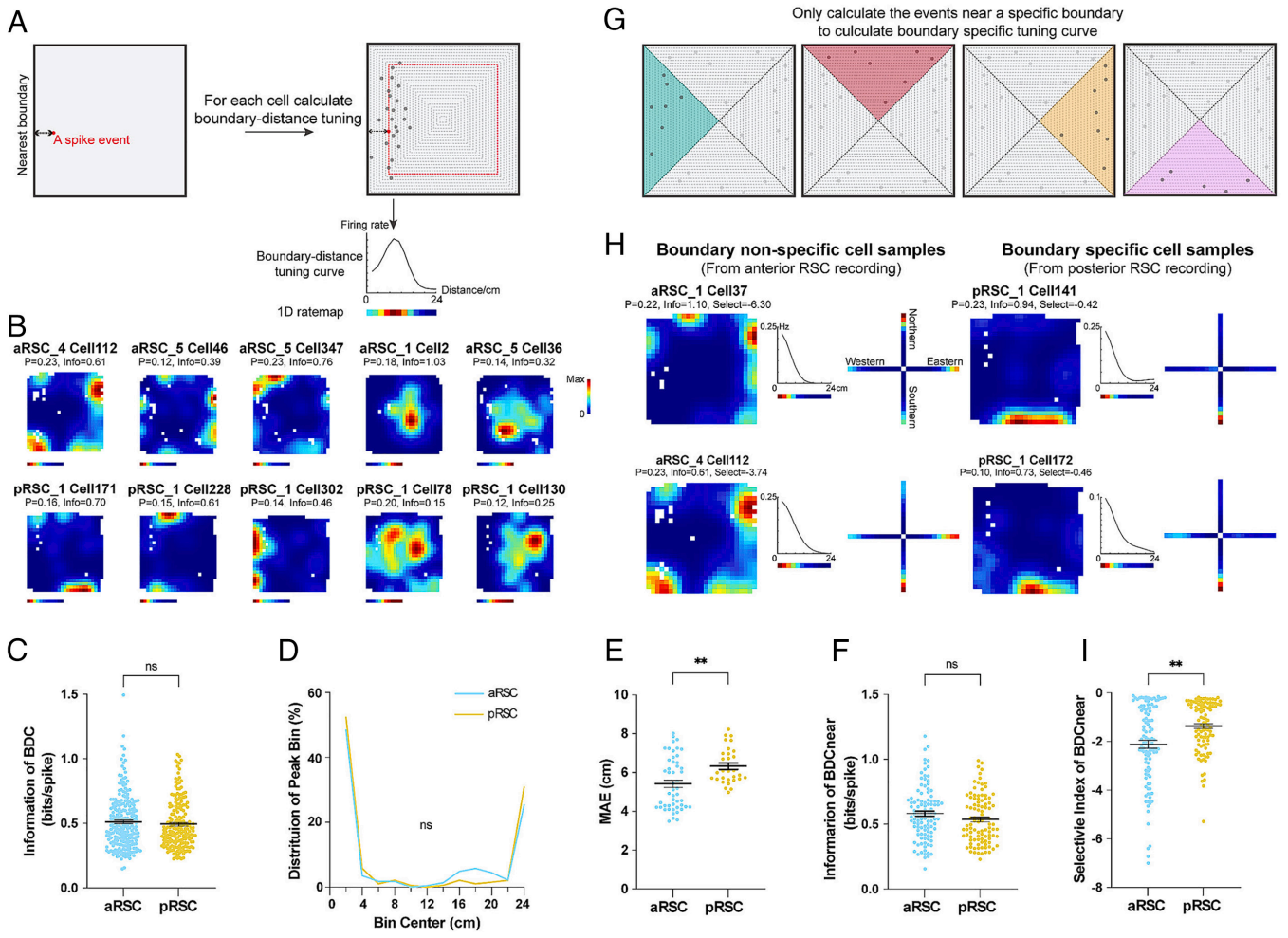


Fig. 2. The properties of BDC and the related boundary selective differences between anterior and posterior RSC. (*A*) The illustration of the calculation of boundary-distance tuning. Gray dashed line: boundary distance bin. Red dashed line: a specific boundary-distance bin. (*B*) BDC samples. *Upper*: 2D ratemap. *Lower*: 1D overall ratemap calculated by boundary distance bins. P: peak rate. Info: spatial information in 1D ratemap. (*C* and *D*) The comparisons of the properties of BDC between anterior and posterior RSC. (*C*) Spatial information of BDCs on 1D ratemap (Welch's *t* test, $P = 0.3468$). (*D*) Peak bin distribution on boundary distance (Kolmogorov–Smirnov test, $P = 0.8183$). (*E*) MAE of decoding using 50 random cells in each session (Mann–Whitney test, $P = 0.0028$). (*F*) Spatial information of BDCnears on 2D ratemap (Welch's *t* test, $P = 0.0965$). (*G*) Illustration of the 4 subfields in a square open field divided by the nearest boundary. The 4 triangle fields filled with different colors represents the 4 subfields separately. (*H*) Cell samples of boundary nonspecific BDCnear and boundary specific BDCnear. *Left* of each cell sample: 2D ratemap. *Inset*: boundary-distance tuning curve and 1D ratemap (the same format as in panel *A* and *B*). *Right* of each cell sample: 1D ratemap in 4 subregions separately. Select: selectivity index. (*I*) Selectivity Index of BDCnears (Mann–Whitney test, $P = 0.0031$).

A Transformation from Egocentric to Allocentric Coding in Anterior to Posterior Boundary Circuits. This integration bias was particularly pronounced in boundary-selective BDCnear populations, supporting their role in representational transformation. Returning to the EBVC×HDC boundary-selectivity hypothesis, we examined allo HD effecting strength in BDCnear populations. Indeed, posterior BDCnear showed stronger allo HD input dependence and weaker ego input modulation than anterior counterparts (Fig. 3 *I* and *J*). Similarly, at the single-cell level of sensitivity to allo HD/ego inputs, the anterior BDCnear population showed no significant differences in response to the exclusion of allo HD or ego information inputs, whereas such differences were observed in the posterior BDCnear population, indicating that posterior BDCnear cells exhibit a stronger bias in their dependency on allo HD/ego information (*SI Appendix*, Fig. S4*F*). Furthermore, the distribution of info-dependent bias in posterior BDCnear cells displayed a significant leftward shift compared to that of anterior BDCnear cells (*SI Appendix*, Fig. S4*G*). These findings suggest that posterior BDCnear cells likely inherit the properties of EBVCs enriched for allocentric HD information processing, thereby developing a more allocentric-biased boundary representation.

Enhanced Boundary Selectivity in pRSC Arises from Integration of Allocentric Head Direction Signals. We next asked how pRSC achieves this enhanced integration. We found that while the basic properties of pure HDCs were similar across subregions (*SI Appendix*, Fig. S5*A*), the EBVC×HDC conjunctive cells in pRSC were functionally superior. This was evidenced by their significantly higher reliance on allo HD input compared to their anterior counterparts (Fig. 4*A*). Consistently, conjunctive cells in pRSC exhibited significantly higher mean vector length (MVL) and stability for allocentric HD tuning compared to both anterior conjunctive cells and pure HDCs within pRSC (Fig. 4 *B* and *C* and *SI Appendix*, Fig. S5*B*). This functional enhancement of allocentric HD coding was specific to conjunctive cells and not seen in the overall population (Fig. 4 *A*–*C*), suggesting that pRSC selectively recruits cells with higher-quality allocentric HD information for conjunctive encoding.

This superiority directly translated to function. We compared conjunctive cells to pure cell types within each subregion. The proportion of conjunctive cells in the HDC and EBVC population was significantly lower in pRSC than in aRSC (Fig. 4 *D* and *G*), although the difference was small (chi-squared test, $P = 0.0257$).

Downloaded from https://www.pnas.org by PEKING UNIVERSITY on August 3, 2026 from IP address 222.29.65.227.

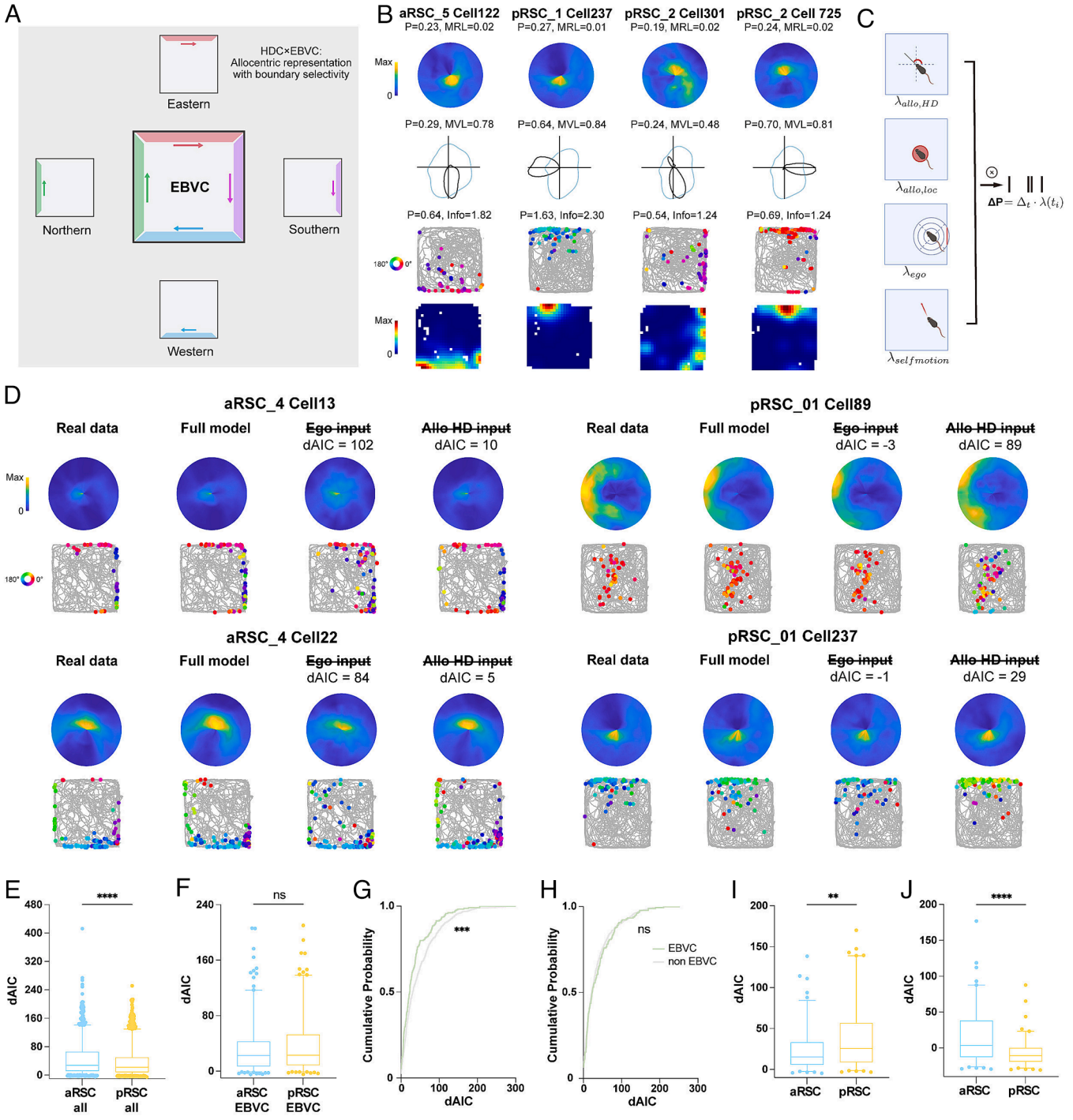


Fig. 3. GLM shows anterior and posterior EBVC differently influenced by allo HD and ego information input. (*A*) Illustration of the reasoning that EBV × HD tuning will lead to a boundary specific firing pattern in allocentric 2D ratemap. The central square represents a typical discharge pattern of an EBVC. The squares within the surrounding gray-shaded regions depict discharge patterns of head-direction cells, specifically tuned to different directional preferences (indicated by the labels below each square). (*B*) Cell samples of conjunctive cells. *Top* of each cell: ratemap in egocentric coordinate. *Second*: head direction tuning curve (black curve), and head direction distribution curve in the whole session (gray curve). *Third*: firing events plot colored by the corresponding head direction. *Bottom*: 2D ratemap. (*C*) The frame of the GLM used on the data. (*D*) GLM predicted neural activity of sample cells. *First* row: ratemap in egocentric coordinate. *Second* row: firing events plot colored by the corresponding head direction. Colume: 1) Real data, 2) Full model, 3) Egocentric input excluded, 4) Allocentric HD input excluded. (*E*) dAIC between anterior and posterior total neuron population when allocentric HD input is excluded from the model (Mann–Whitney test, $P < 0.0001$). (*F*) dAIC between anterior and posterior EBVC population when allocentric HD input is excluded from the model (Mann–Whitney test, $P = 0.3849$). (*G*) Cumulative distribution curve of dAIC of anterior EBVC and nonEBVC when allocentric HD input is excluded from the model (Kolmogorov–Smirnov test, $P = 0.0001$). (*H*) Cumulative distribution curve of dAIC of posterior EBVC and nonEBVC when allocentric HD input is excluded from the model (Kolmogorov–Smirnov test, $P = 0.4127$). *Inset*: Box plot of the two groups of data (Mann–Whitney test, $P = 0.3272$). (*I*) dAIC between anterior and posterior BDCnear population when allocentric HD input is excluded from the model (Mann–Whitney test, $P = 0.0077$). (*J*) dAIC between anterior and posterior BDCnear population when egocentric input is excluded from the model (Mann–Whitney test, $P < 0.0001$).

Importantly, the key functional difference emerged in pRSC. Here, conjunctive cells were functionally superior to pure HDCs and EBVCs (Fig. 4*H*). This enhancement directly translated to function, as conjunctive cells within the pRSC BDCnear population exhibited a significantly higher boundary selectivity index than their nonconjunctive counterparts (Fig. 4*I*). In contrast, no

Downloaded from https://www.pnas.org by PEKING UNIVERSITY on August 3, 2026 from IP address 222.29.65.227.

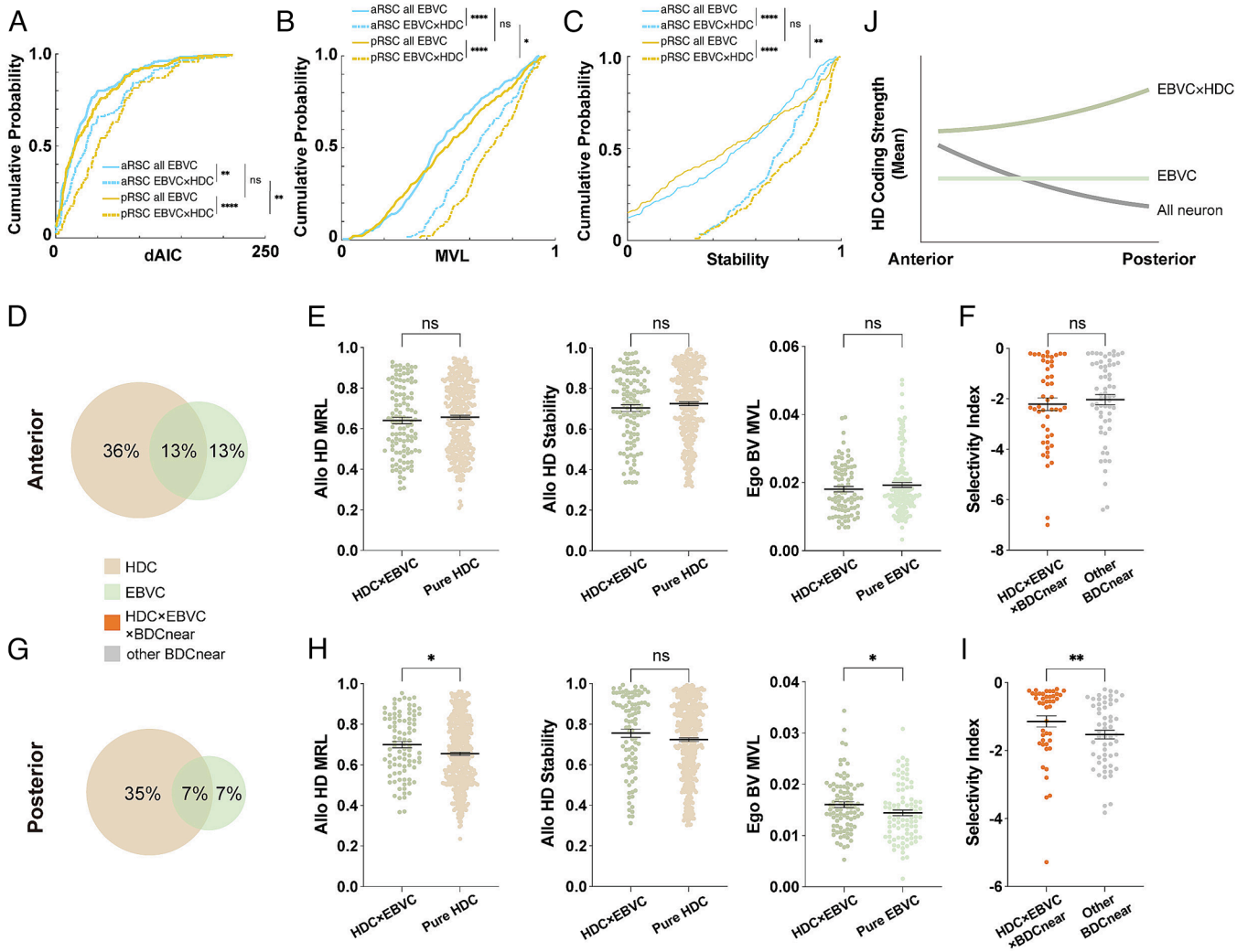


Fig. 4. Integration of better local egocentric and allocentric information leads to allocentric boundary selectivity of pRSC neurons. (*A*) Cumulative distribution curve of GLM dAIC with allo HD input excluded of all EBVC and conjunctive EBVC in both anterior and posterior population (Kolmogorov–Smirnov test. Anterior all vs. EBVC×HDC, $P = 0.0055$. Posterior all vs. EBVC×HDC, $P < 0.0001$. Anterior EBVC vs. posterior EBVC, $P = 0.1982$. Anterior EBVC×HDC vs. posterior EBVC×HDC, $P = 0.0097$). (*B*) Cumulative distribution curve of MVL (allocentric direction tuning) of all EBVC and conjunctive EBVC in both anterior and posterior population (Kolmogorov–Smirnov test. Anterior all vs. EBVC×HDC, $P < 0.0001$. Posterior all vs. EBVC×HDC, $P < 0.0001$. Anterior EBVC vs. posterior EBVC, $P = 0.3591$. Anterior EBVC×HDC vs. posterior EBVC×HDC, $P = 0.0366$). (*C*) Cumulative distribution curve of head direction tuning stability of all EBVC and conjunctive EBVC in both anterior and posterior population (Kolmogorov–Smirnov test. Anterior all vs. EBVC×HDC, $P < 0.0001$. Posterior all vs. EBVC×HDC, $P < 0.0001$. Anterior EBVC vs. posterior EBVC, $P = 0.1424$. Anterior EBVC×HDC vs. posterior EBVC×HDC, $P = 0.0071$). (*D*) Proportion of HDC, EBVC, and the conjunction of both in the total cell population of the recording in aRSC. (*E*) The comparison of HDC × EBVCs and pure HDCs or EBVCs in aRSC. *Left*: MRL of allocentric head direction tuning of HDC × EBVCs and pure HDCs (Welch's *t* test, $P = 0.3724$). *Middle*: Stability of allocentric head direction tuning of HDC × EBVCs and pure HDCs (Welch's *t* test, $P = 0.2608$). *Right*: MVL of egocentric boundary vector tuning (Welch's *t* test, $P = 0.2615$). (*F*) Selectivity index of BDCnears conjunct with EBV × HD tuning and other BDCnears in aRSC (Mann–Whitney test, $P = 0.5411$). (*G*–*I*) Same as *E* and *F*, but in the pRSC. (*H*) *Left*, Welch's *t* test, $P = 0.0116$. Middle, Welch's *t* test, $P = 0.1418$. *Right*, Welch's *t* test, $P = 0.0384$. (*I*) Mann–Whitney test, $P = 0.0069$). (*J*) The schematic diagram illustrates the differences of allocentric head direction coding strength along the anteroposterior axis across different cell populations.

such enhancement was found in aRSC (Fig. 4 *E* and *F*). This indicates that pRSC dedicates a specialized population of high-fidelity conjunctive cells, resulting in a more selective boundary representation.

These findings demonstrate that higher-quality conjunctive cells do effectively enhance firing selectivity, providing partial validation for our proposed mechanism underlying the formation of boundary selectivity (Fig. 3*A*). The key distinction between aRSC and pRSC lies in their coding strategies: in the anterior region, allocentric HD coding and egocentric boundary coding tend to be more separated, whereas EBVCs in the posterior region partially integrate allocentric information, which ultimately converges onto conjunctive cells. This mechanism may enable allocentric coding to be highly concentrated in conjunctive cells, thereby enhancing the efficiency and specificity of coding information (Fig. 4*J*).

Population-level analyses further confirmed the enhanced conjunctive coding and boundary selectivity in pRSC. Under the aforementioned logical framework, when comparing the selectivity index of the whole conjunctive population, it is evident that the posterior region exhibits a significantly higher index than the anterior region (*SI Appendix*, Fig. S5*C*). This also provides evidence suggesting that enhanced conjunctive properties may lead to improved boundary selectivity. Furthermore, consistent evidence was found in the comparison of the selectivity index among BDCnear cells (*SI Appendix*, Fig. S5*D*).

Neurons Exhibiting Global Tuning Properties Are Enriched among RSC→MEC Projection Neurons Relative to the Total pRSC Population. We then recorded RSC→MEC neuron population (*SI Appendix*, Fig. S1*C*) and characterized the functional properties

Downloaded from https://www.pnas.org by PEKING UNIVERSITY on August 3, 2026 from IP address 222.29.65.227.

of the pRSC subpopulation that projects to the MEC (Figs. 5 and 6 and *SI Appendix*, Fig. S6). We found that the RSC→MEC pathway is enriched for conjunctive coding and exhibits a distinct "global" tuning profile.

From the perspective of egocentric coding, EBVCs in this projecting population showed significantly higher MRL for egocentric boundary coding compared to the general pRSC population (Fig. 5 *A* and *I*). However, this enhancement in coding strength was accompanied by broader spatial tuning: EBVCs had larger field sizes (Fig. 5*B*), BDCs displayed lower spatial information (Fig. 5*C*) and wider field width (Fig. 5*D*). HDCs exhibited broader directional tuning (Fig. 5*E*) and higher coding stability (Fig. 5*F*), despite showing comparable MVL (Fig. 5*G*).

Our analysis of allocentric coding primarily focused on the properties of BDC. In terms of coding precision along this dimension, RSC→MEC BDCnears did not demonstrate higher boundary selectivity compared to the total BDC population (Fig. 5*H*). However, it appears that they still possess boundary selectivity, but due to the relatively broad tuning width, this selectivity might not manifest as a significant increase in the selectivity index (*SI Appendix*, Fig. S7*A*).

We reasoned that their boundary selectivity might reflect a "global" coding strategy, which shows more responses to a specific boundary (Fig. 5*J*), rather than a "local" strategy of responding to every of the 4 boundaries with a specific egocentric relationship (13, 34, 35) (Fig. 5*K* and *SI Appendix*, Fig. S7*B*). Analysis of

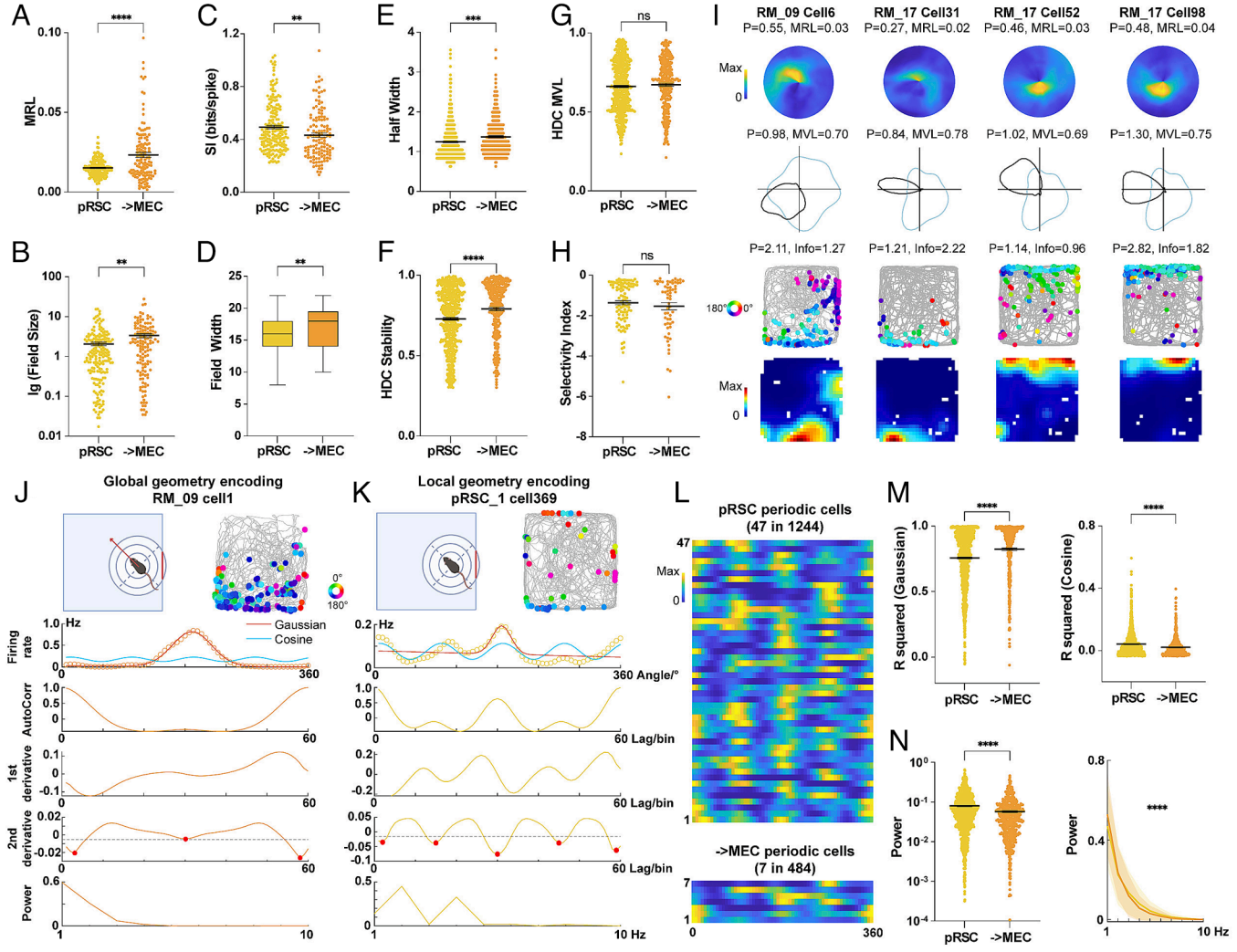


Fig. 5. The comparisons of the quality of functional neuron types and periodic property between pRSC total and RSC→MEC subpopulation. (*A* and *B*) The comparisons of the properties of EBVC between pRSC total population and the RSC→MEC subpopulation. (*A*) MRL of EBVCs (Welch's *t* test, $P < 0.0001$). (*B*) Logarithmic field size in egocentric ratemap of EBVCs (Welch's *t* test, $P = 0.0029$). (*C* and *D*) The comparisons of the properties of BDC between pRSC total population and the RSC→MEC subpopulation. (*C*) Spatial information of BDCs in 1D ratemap (Welch's *t* test, $P = 0.0036$). (*D*) Field width of BDCs in 1D ratemap (Welch's *t* test, $P = 0.0059$). (*E*–*G*) The comparisons of the properties of HDC between pRSC total population and the RSC→MEC subpopulation. (*E*) Half width of HD tuning curve of HDCs (Welch's *t* test, $P = 0.0001$). (*F*) Half-half stability of HDCs (Welch's *t* test, $P < 0.0001$). (*G*) MVL of HDCs (Welch's *t* test, $P = 3794$). (*H*) Selectivity Index of BDCnears (Mann–Whitney test, $P = 0.4968$). (*I*) Cell samples of conjunctive cells recorded in RSC→MEC subpopulation. (*J*) The illustration and a cell sample of global geometry encoding. *Upper Left:* the illustration of the concept of global geometry encoding. *Upper Right*: the firing events plot of a sample periodic cell, colored by the corresponding head direction. Lower, each row: 1) The head direction tuning curve of the sample cell, aligning with the fitted result of Gaussian (red) and cosine (blue) function. 2) The autocorrelation of the tuning curve. 3) The 1st derivative of the autocorrelation curve. 4) The 2nd derivative of the autocorrelation curve. Dashed line: the 20% of the minimum negative value. 5) The power of the first 10 components of Fourier transform. The x axis represents the corresponding frequency of the first 10 components. (*K*) Same as *J*, but for a local geometry encoding cell sample. (*L*) Rate map of all periodic cells classified in pRSC total population and RSC→MEC population, aligned by the phase of the fitted cosine function. (*M*) The comparisons of the goodness of fit by Gaussian of cosine function in pRSC and RSC→MEC population. *Left*: R squared fit by Gaussian distribution (Mann–Whitney test, $P < 0.0001$). *Right*: R squared fit by cosine function (Mann–Whitney test, $P < 0.0001$). (*N*) The comparisons of the power of the 4th component calculated by Fourier transformation in pRSC total population and RSC→MEC population. *Left*: The power of 4th component (Mann–Whitney test, $P < 0.0001$). *Right*: The mean with STD of all cells in the two populations among the first 10 components calculated by Fourier transformation. Line: average value. Shadow: ±STD (Kolmogorov–Smirnov test, $P < 0.0001$).

Downloaded from https://www.pnas.org by PEKING UNIVERSITY on August 3, 2026 from IP address 222.29.65.227.

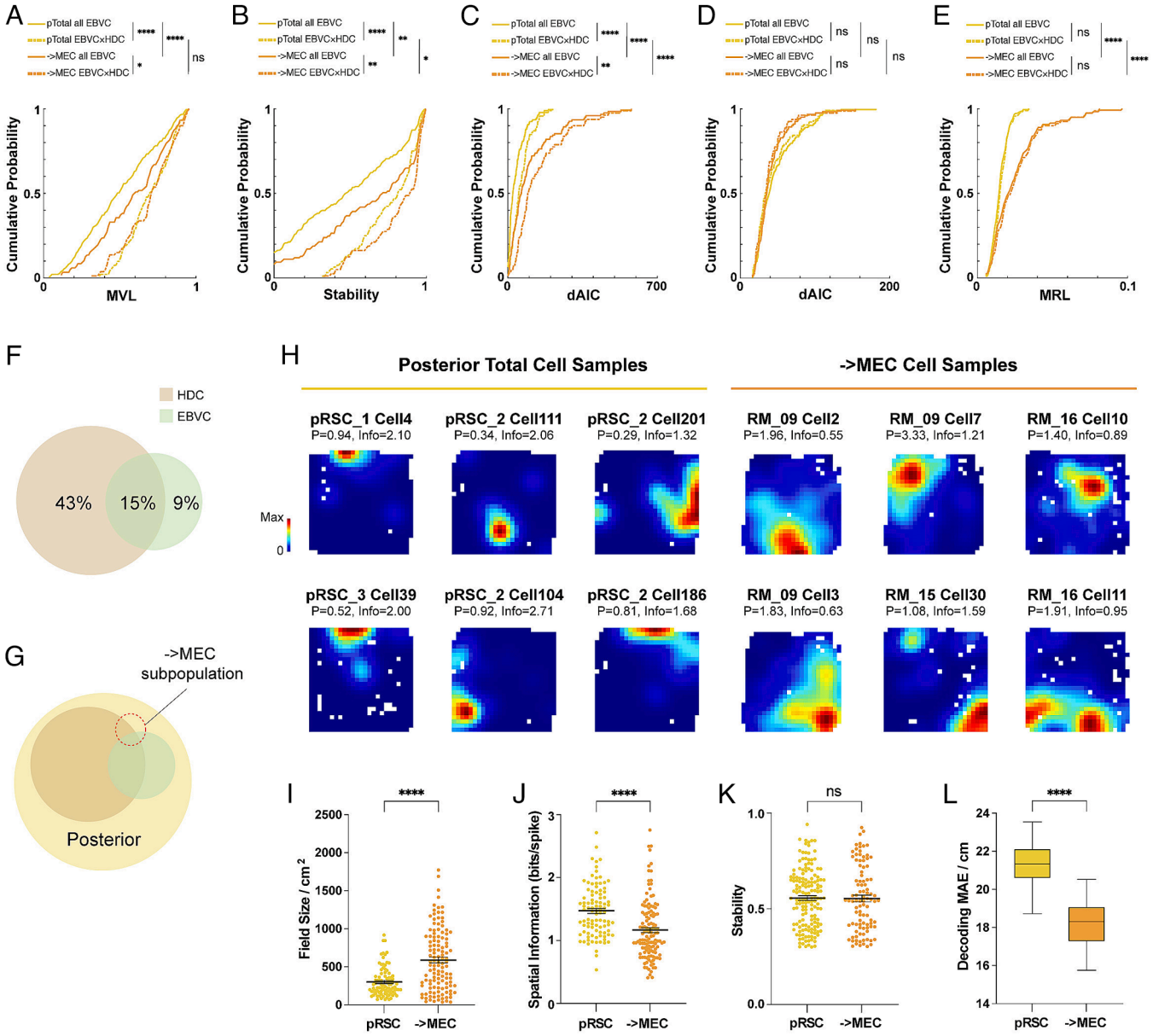


Fig. 6. The EBVCs projecting to MEC brings better allocentric direction information, and further show enriched allocentric spatial coding. (*A*) Cumulative distribution curve of MVL (allocentric direction tuning) of all EBVC and conjunctive EBVC in both pRSC total population and RSC→MEC population (Kolmogorov–Smirnov test. Posterior all vs. EBVC×HDC, $P < 0.0001$. RSC→MEC all vs. EBVC×HDC, $P = 0.0294$. Posterior EBVC vs. RSC→MEC EBVC, $P < 0.0001$. Posterior EBVC×HDC vs. RSC→MEC EBVC×HDC, $P = 0.6150$). (*B*) Cumulative distribution curve of head direction tuning stability of all EBVC and conjunctive EBVC in both pRSC total population and RSC→MEC population (Kolmogorov–Smirnov test. Posterior all vs. EBVC×HDC, $P < 0.0001$. RSC→MEC all vs. EBVC×HDC, $P = 0.0036$. Posterior EBVC vs. RSC→MEC EBVC, $P < 0.0064$. Posterior EBVC×HDC vs. RSC→MEC EBVC×HDC, $P = 0.0263$). (*C*) Cumulative distribution curve of GLM dAIC with allo HD input excluded of all EBVC and conjunctive EBVC in both pRSC total population and RSC→MEC population (Kolmogorov–Smirnov test. Posterior all vs. EBVC×HDC, $P < 0.0001$. RSC→MEC all vs. EBVC×HDC, $P = 0.0070$. Posterior EBVC vs. RSC→MEC EBVC, $P < 0.0001$. Posterior EBVC×HDC vs. RSC→MEC EBVC×HDC, $P < 0.0001$). (*D*) Cumulative distribution curve of GLM dAIC with ego input excluded of all EBVC and conjunctive EBVC in both pRSC total population and RSC→MEC population (Kolmogorov–Smirnov test. Posterior all vs. EBVC×HDC, $P = 0.6555$. RSC→MEC all vs. EBVC×HDC, $P = 0.9683$. Posterior EBVC vs. RSC→MEC EBVC, $P = 0.00893$. Posterior EBVC×HDC vs. RSC→MEC EBVC×HDC, $P = 0.2695$). (*E*) Cumulative distribution curve of MRL (egocentric boundary vector coding) of all EBVC and conjunctive EBVC in both pRSC total population and RSC→MEC population (Kolmogorov–Smirnov test. Posterior all vs. EBVC×HDC, $P = 0.7838$. RSC→MEC all vs. EBVC×HDC, $P = 0.9890$. Posterior EBVC vs. RSC→MEC EBVC, $P < 0.0001$. Posterior EBVC×HDC vs. RSC→MEC EBVC×HDC, $P < 0.0001$). (*F*) Proportion of HDC, EBVC, and the conjunction of both in the recording of RSC→MEC subpopulation. The format is the same as panel F in Fig. 4. (*G*) The schematic illustration of the proportion of HDC and EBVC conjunction in the pRSC total population, and the concentrated proportion in the RSC→MEC subpopulation. (*H*) PC samples from pRSC total population and RSC→MEC subpopulation. (*I–K*) Comparisons of place cells in pRSC total population and RSC→MEC subpopulation. (*I*) Field size (Welch's *t* test, $P < 0.0001$). (*J*) Spatial information (Welch's *t* test, $P < 0.0001$). (*K*) Stability (Welch's *t* test, $P = 0.6937$). (*L*) MAE of decoding using 50 random cells in each session (Mann–Whitney test, $P < 0.0001$).

periodicity in subpopulation of neurons tuning curves confirmed this: the general pRSC population had more cells with 4-fold periodic firing (a local code), while the RSC→MEC population was biased toward nonperiodic, global coding (Fig. 5 *L–N*). Crucially, the properties of egocentric-to-allocentric transformation, as defined previously by periodicity, are also reflected in EBVC and BDCnear (*SI Appendix*, Fig. S7 *C–F*). Together, through both selectivity analysis and periodic fitting approaches, our results provide complementary evidence for distinct egocentric versus allocentric encoding biases across different cell populations.

The RSC→MEC Pathway Recruits EBVCs with Superior Allocentric Information for Efficient Spatial Mapping. Finally, we investigated the functional consequence of this specialized projection. Within the RSC→MEC pathway, EBVCs possessed significantly higher-quality allocentric HD information (higher MVL) and coding

Downloaded from https://www.pnas.org by PEKING UNIVERSITY on August 3, 2026 from IP address 222.29.65.227.

stability than EBVCs in the general pRSC population (Fig. 6 *A* and *B*). Surprisingly, we found that the disparity in allocentric head direction information quality primarily manifested in the overall EBVC population rather than specifically in the EBVC×HDC conjunctive subpopulation (Fig. 6 *A* and *B* and *SI Appendix*, Fig. S8 *A* and *B*). GLM analysis confirmed that RSC→MEC EBVCs and conjunctive cells depended more on allo HD inputs (Fig. 6 *C* and *D*), aligning with their global coding suf (*SI Appendix*, Fig. S8*E*).

Regarding egocentric coding in both EBVCs and conjunctive cells, the substantial differences between pRSC total and RSC→MEC populations were similarly reflected in their respective conjunctive cell populations (Fig. 6*E* and *SI Appendix*, Fig. S8*C*).

In terms of proportion, the conjunction proportion in RSC→MEC proportion is significantly higher (chi-squared test, $P = 0.0057$) than that in pRSC total population (Figs. 4*G* and 6*F*).

These findings demonstrate that the differences in allocentric coding within the RSC to MEC pathway primarily manifest in the EBVC population: RSC selectively 1) projects EBVCs containing higher allocentric information to MEC and 2) enriches conjunctive information in its projections to MEC (Fig. 6 *F* and *G*).

Although their egocentric tuning was broader, the strong integration of allocentric information endowed a larger fraction of RSC→MEC conjunctive cells with allocentric spatial coding properties. 44/80 conjunctive cells in RSC→MEC population vs. 29/92 conjunctive cells in general pRSC are classified as PC (Fig. 6*H*). This suggests that although the superior egocentric boundary coding ability of RSC→MEC conjunctive cells did not result in higher boundary selectivity (*SI Appendix*, Fig. S8*D*), it may have endowed a larger fraction of these cells with enhanced allocentric 2D spatial representation capabilities.

These PCs had larger place fields and lower spatial information than those in pRSC total population (Fig. 6 *I* and *J*), consistent with the overall broad tuning of the pathway, while no significant differences were observed in stability (Fig. 6*K*). Notably, when decoding the animal's position using randomly selected subsets of cells matched in number across sessions, the RSC→MEC population demonstrated lower decoding accuracy (Fig. 6*L*). This is likely attributable to the significantly higher proportion of PCs in the RSC→MEC population, which, despite their lower individual precision, collectively enhance the subpopulation's coding efficiency for spatial location through their enriched representation.

In essence, the RSC→MEC pathway, which recruits a larger proportion of functional cell types, is optimized to provide MEC with a spatially integrated, globally referenced representation built from broadly tuned but highly conjunctive inputs, rather than a collection of precise local signals.

Discussion

This study provides a comprehensive functional dissection of the RSC, revealing fundamental anterior-to-posterior differences in spatial coding strategies. We demonstrate that the pRSC, and particularly its MEC-projecting subpopulation, is specialized for high-fidelity conjunctive coding. This integrative process merges egocentric and allocentric information to generate a transformed, boundary-selective representation of space. Our findings thus resolve long-standing questions regarding the internal organization of the RSC and clarify its specific computational role within the navigation network.

Functional Differences of Conjunctive Coding in the RSC. Our investigation reveals distinct functional differences along the RSC's anteroposterior axis (Figs. 1–4). While neurons with spatial tuning are present throughout the RSC, pRSC neurons exhibit significantly stronger multimodal integration and conjunctive coding capabilities compared to their anterior counterparts (Figs. 3 and 4). Regarding the source of this difference, we propose two possible aspects.

This differentiation could partially stem from distinct connectivity profiles: the aRSC maintains dense connections with prefrontal regions (36), supporting contextual processing, whereas pRSC receives robust visual-spatial inputs (37–40). This anatomical divergence underpins their differential roles in cognition, as evidenced by studies showing that inhibition of pRSC versus aRSC selectively impairs contextual versus cue-associated memory (41), respectively. The functional specializations we observe likely arise from, and are refined by, these unique input–output architectures mentioned above. Notably, projection-specific neurons within the RSC are known to receive inputs from distinct upstream sources (17). Future work investigating whether MEC-projecting neurons receive specialized afferents will be crucial for fully elucidating the mechanisms underlying their functional enrichment.

In addition to possibly arising from connectivity patterns, we also propose another possibility. The functional differences may not entirely originate from a gradient of functional inputs to RSC. Given that pRSC is a core hub for outputting spatial information to MEC, we hypothesize that within RSC, there may be a computational strategy gradient along the anterior–posterior axis. Specifically, pRSC may be more inclined to integrate widely distributed egocentric and allocentric inputs from the brain into higher-order allocentric signals required by MEC.

From Egocentric Sensing to Allocentric Mapping: The Transformative Role of pRSC. Our results indicate that pRSC does not merely encode distance to arbitrary boundaries but rather computes the identity of specific boundaries within an allocentric framework (Figs. 1 and 3). This provides crucial cellular-level evidence for the RSC's hypothesized role as a coordinate transformation hub. We precisely localize this function to the posterior subdivision, and particularly to its boundary-proximal cells (BDCnear), whose high boundary selectivity resembles that of classical boundary cells in MEC (Figs. 5 and 6), suggesting pRSC as a key upstream source of allocentric boundary signals.

The cellular mechanism for this transformation involves the enhanced integration of allocentric HD information. Our GLM analyses reveal a systematic shift in input dependency along the anteroposterior axis (Fig. 3): EBVCs in aRSC rely more on egocentric boundary vector inputs, whereas those in pRSC show stronger dependence on allocentric HD inputs. This integration is particularly refined in specialized EBVC×HDC conjunctive cells within pRSC (Fig. 3). This conjunctive mechanism effectively transforms a viewer-centered vector (e.g., "boundary to my left") into a world-anchored landmark signal (e.g., "the north wall"), thereby sharpening boundary identity selectivity.

We propose that this transformative computation is most critical during the initial formation of allocentric cognitive maps. The pRSC→MEC pathway may thus provide an instructive signal to help anchor nascent spatial representations in the parahippocampal formation. Once an environment becomes familiar and MEC representations stabilize, RSC's inputs may transition to a modulatory or feedback role for fine-tuning, rather than fundamentally instructing the established map. This could explain why inhibiting RSC has limited immediate impact on well-formed boundary representations in MEC (42), without contradicting its potential role in spatial memory retrieval or map initialization.

Downloaded from https://www.pnas.org by PEKING UNIVERSITY on August 3, 2026 from IP address 222.29.65.227.

Circuit Mechanisms and Future Perspectives. Our in-depth analysis of the pRSC→MEC circuit underscores the necessity of deconstructing RSC function from a precise, circuit-specific perspective. As a critical hub, its computational roles are defined by unique "input-processing-output" motifs. Consequently, future research must extend beyond describing the RSC as a unitary entity in spatial memory. Priorities should include: 1) employing projection-specific manipulations during novel environment exploration to causally test the instructive role of the pRSC→MEC pathway; 2) conducting simultaneous cross-regional recordings to delineate real-time information flow between pRSC and MEC; and 3) mapping the complete upstream inputs that drive these specialized neuronal subpopulations to close the functional loop. Additionally, further study should also dig into the internal coding structure of the RSC. Employing tetrode recordings or other methods to achieve higher-resolution histological dissection will help distinguish the layer-specific functional distribution of the RSC, thereby furthering our understanding of its hub function.

Understanding these circuit-specific mechanisms holds profound scientific significance. It is essential for revealing how the brain constructs a stable representation of space from transient sensory inputs. Moreover, given the RSC's early vulnerability in Alzheimer's disease (43–45), elucidating these precise computational circuits in mice provides a valuable reference helping to understand the neural basis in human diseases.

Materials and Methods

Subjects. In this study, 12 male C57BL/6 wild-type mice were used. All procedures for animals were approved by Animal Care and Use Committee of Peking University. All mice were individually housed under a 12 h light/dark cycle at a temperature of 22 °C and provided with food and water continuously. A running wheel was placed in the cage to enhance the mice's activity. Behavioral experiments were all conducted during the dark phase. During the training and recording period, the mice were food-restricted to keep at 90% of their weight during free feeding. All mice were aged at 9 to 12 wk prior to the surgery.

Surgery. Mice were anesthetized with isoflurane and placed in a stereotaxic instrument (KOPF). For local imaging of anterior/posterior RSC, rAAV-hSyn-GCaMP6f-WPRE-hGh was injected using a glass pipette (NANOLITER2020 Injector, World Precision Instruments, FL).

For aRSC, we injected two sites, −0.4 mm ML, +1.1/1.4 mm anterior to the transverse sinus, −0.8 mm DV, each site with 150 nL virus at a rate of 80 nL/min. At each injection site, the glass pipette was left in place for 10 min before retraction. After the virus injection, we then began to implant prism. The imaging lens consists of a customized 1 mm side-length GRIN (gradient-index) lens attached to a 1 mm square prism (Grintech, Germany). The prism was implanted vertically into the brain. The coordinate of prism implantation was −0.7 mm ML, +0.8 mm anterior to the transverse sinus, −1 mm DV.

For pRSC, we injected two sites, −2.4 mm ML, +0.3/+0.7 mm anterior to the transverse sinus, −0.8 mm DV, each site with 150 nL virus at a rate of 80 nL/min. The coordinate of prism implantation was −2.65 mm ML, with the posterior edge adjacent to the transverse sinus, −1 mm DV.

For RSC→MEC neuron imaging, we injected rAAV-hSyn-GCaMP6s-WPRE-hGH polyA with 2/R serotype into the MEC. We injected two sites, −3.2 mm ML, 0.3 mm anterior to the transverse sinus, −1.8 to −1.6 mm DV and −3.6 mm ML, 0.3 mm anterior to the transverse sinus, −1.6 to −1.4 mm DV, each site with 400 nL virus at a rate of 80 nL/min. The prism was implanted at the same coordinate as pRSC imaging surgery.

After the implantation, the Kwik-Cast (World Precision Instruments, FL) was used to cover the chronic window. Tissue adhesive (3 M, MN) was used to bond the scalp to the skull. To secure the miniaturized two-photon probe, a headplate was implanted on the mouse skull, and the gap between the headplate and the skull was filled with dental cement. After a 2 to 3 wk recovery period, we were able to observe calcium signals using the miniaturized two-photon probe.

Behavioral Training and Recording in Open-Field Test. The experiment was conducted in a square open-field arena (50 cm side length) with white flooring and black walls (40 cm high). A white A4-sized cue card was attached to one wall as the primary spatial landmark, while black curtains surrounded the arena to minimize distal visual cues. Illumination was provided by dim white LED lighting to ensure visibility without compromising imaging quality, supplemented by infrared lighting for behavioral video recording.

Prior to testing, mice underwent food restriction to maintain body weight at ~80% of baseline. They were habituated to the arena over 1 to 2 wk under consistent baseline conditions (fixed cue card position), with cookie crumbs used as rewards to encourage free exploration. In the final stage of training the mice, when they achieve over 90% coverage in the box during a 10-min session and maintain this performance in two consecutive training sessions, we consider their behavior to be sufficient for recording. During recording, each mouse performed two consecutive 10-min trials per day under identical conditions, with a 5- to 10-min rest in the home cage between trials. Behavioral data from both trials were concatenated for analysis, yielding a continuous 20-min dataset per session.

Two-Photon Calcium Imaging. Neuron activity was recorded by a miniaturized 2-photon microscope (LFMTPM V2.0.1, Transcend Vivoscope Biotech Co., Ltd., China; Working distance: ~1 mm; Numerical aperture: 0.45 mm).

Before calcium signal recording, we first identified the field of view (FOV) and affixed a baseplate to the headplate to ensure stable imaging. Following confirmation of appropriate viral expression and calcium signals in the mouse brain, we implanted a headplate to stabilize the imaging probe position, enabling consistent targeting of the same FOV across sessions. Imaging was performed at 600 × 512 pixels resolution with ~0.89 μm/pixel size and ~9 Hz frame rate using GINKGO-MTPM software (Transcend Vivoscope Biotech Co., Ltd, China). For mice with signal regions smaller than one FOV, we used data from a single imaging session. When multiple FOVs were required, we sequentially recorded from nonoverlapping regions by repositioning the headplate between sessions, with each FOV treated as an independent dataset while maintaining identical behavioral paradigms.

During recording, we filled the headplate well with hydrogel to maintain aqueous immersion and avoided any probe adjustments mid-session to ensure FOV stability. The two-photon calcium imaging was performed using 920 nm excitation wavelength. The behavioral recording was simultaneously acquired using an infrared camera at 30 Hz frame rate. All neural and behavioral data streams were synchronized through hardware-generated timestamps.

Process of Calcium Data. Neurons and their fluorescence signal fluctuations were extracted using Suite2p (46) to identify the spatial footprints (SFP) of neurons and obtain corresponding ΔF/F signals. The fluorescence signals were then deconvolved using OASIS (47) to detect spiking events for each neuron. Detected events were filtered by applying a threshold of >1 SD above baseline, and the corresponding frames of the filtered events were identified as neuronal spikes. Behavioral and imaging data were aligned using timestamps, and the behavioral frame closest to each spike was used to determine the associated behavioral event features.

Behavioral Analyses. Mouse behavioral data were extracted from behavioral videos using DeepLabCut (48). The animal's position, head direction, and velocity were further calculated using custom Matlab scripts. For analysis, the 50 × 50 cm open field arena was spatially divided into 2 cm-side bins. Behavioral coverage and corresponding neuronal firing activity were computed for each individual bin.

Classification of Functional Cell Types. We calculated the firing properties of all recorded neurons, and classified functional neurons as head direction cell, egocentric boundary vector cell, boundary distance cell, speed cell, angular head velocity cell and place cell.

Here we only introduce the specific judgment method for BDC. The other five cell types are similar to common calculation methods and are provided in the *SI Appendix*.

We analyzed boundary distance coding by establishing 2 cm-spaced distance bins along the arena perimeter (0 to 25 cm range, 12 bins total after excluding the innermost bin). For each neuron, firing rates were calculated per bin to generate boundary distance tuning curves. Neurons were classified as BDCs when their spatial information exceeded the 95th percentile of shuffled distributions. BDCs with peak firing within 6 cm of boundaries (first 3 bins) were designated

Downloaded from https://www.pnas.org by PEKING UNIVERSITY on August 3, 2026 from IP address 222.29.65.227.

BDCnear, while those with peaks in distal bins (>6 cm) and field widths >12 cm (6 bins) were classified BDCfar.

Field width calculations identified firing field boundaries by locating where firing rates either: 1) exceeded a threshold defined as the minimum firing rate plus 10% of the dynamic range (maximum minus minimum firing rate), or 2) showed derivative sign changes (left boundary: dF/dx > 0; right boundary: dF/dx < 0). Stability was assessed via Pearson correlation between first/second trial half tuning curves. Spatial information was computed following the established method (49):

$$\text{Spatial Information}(\text{bits/spike}) = \sum_{i=1}^{N} p_i \frac{\lambda_i}{\lambda} \log_2 \left(\frac{\lambda_i}{\lambda}\right),$$

where i represents each individual spatial bin in the two-dimensional environment, N corresponds to the total number of bins, p_i indicates the occupancy probability for bin i derived from the animal's behavioral trajectory data, λ_i denotes the mean firing rate within bin i calculated as the number of spike events divided by dwell time in that bin, and λ represents the overall mean firing rate across all bins in the environment.

For boundary-specific analysis, spikes were categorized by nearest boundary (4 categories) to generate subregion tuning curves. The selectivity index was calculated as the natural logarithm of the variance of Pearson correlation coefficients between each of the four boundary-specific tuning curves and the overall boundary distance tuning curve.

Overlap Index. We calculated the overlap index (OI) between two cell types following established method (50), where the expected overlap was derived from the product of each cell type's proportion multiplied by the total cell count. The OI was computed as the ratio of observed double-labeled cells to the expected value:

$$OI = m/nab,$$

where proportions a and b representing type A and B abundances respectively. Statistical significance was determined through binomial testing, where OI > 1 ($P < 0.05$) indicated significant co-occurrence exceeding chance, while OI < 1 ($P < 0.05$) revealed significant segregation between cell types.

GLM Model. To analyze egocentric and allocentric inputs separately, we adopt a GLM framework, where the spiking probability is influenced by different variables, including allocentric spatial coding, allocentric head direction coding, egocentric coding, and self-motion.

Egocentric coding consists of the distance to the nearest boundary, denoted as db and the included angle ϕ between the animal's current head direction and the nearest boundary.

Allocentric coding includes the animal's 2D coordinates (x, y) within the environment and its head direction θ.

Self-motion coding is represented by the animal's running speed v and angular head direction speed α of the animal.

We assume that the neuron's spike train follows an inhomogeneous poisson process with an intensity function $\lambda(t)$. Given a series of time points $t_1, t_2, \cdots, t_n$ with corresponding predictors described above determined by the behavior data, the total spike count up to time t_i is denoted as X_i. The probability of a spike occurring within the time bin at $[ti - 1, ti]$ is given by

$$P(X_i - X_{i-1} = 1) = t \cdot \lambda(t_i),$$

where Δt is the length of the time bin. All predictors mentioned below refer to their values at time t_i with the subscript i omitted for brevity.

$$\lambda(t_i) = \beta_{rate} \cdot \lambda_{allo,HD} \cdot \lambda_{allo,loc} \cdot \lambda_{ego} \cdot \lambda_{selfmotion},$$

where

$$\lambda_{allo,HD} = (\sin\ \theta, \cos\ \theta, \sin\ 2\theta, \cos\ 2\theta)^T \beta_{allo,HD},$$

$$\lambda_{allo,loc} = (x, y, x^2, y^2, xy)^T \beta_{allo,loc},$$

$$\lambda_{ego} = (d_b, {d_b}^2,\ \sin\ \phi, \cos\ \phi, d_b\ \sin\ \phi, d_b\ \cos\ \phi)^T \beta_{ego},$$

$$\lambda_{selfmotion} = (v, \alpha)^T \beta_{selfmotion}.$$

Position and Head Direction Decoding. We used naive Bayesian decoding for animal position or head direction estimation. The detailed calculation method is provided in the *SI Appendix*.

Periodic Cell. We determine periodic firing neurons by analyzing the autocorrelation function of neuronal head-direction tuning curves and their derivatives. The criteria for the autocorrelation function curve are as follows: 1) Its second derivative has exactly three local minima (troughs); 2) The first trough is located within bin 0 to 5, the second trough is 13 to 17 bins away from the first, and the third trough is strictly located at bin 30; 3) The value of the second derivative at each trough must be negative and must be less than 20% of the global minimum value. Neurons meeting these criteria are classified as periodic firing neurons; otherwise, they are classified as nonperiodic firing neurons.

We use MATLAB's fitnlm function (nonlinear regression fitting) to fit the head-direction tuning curves with two mathematical models to further assess the periodicity of head-direction modulation. The specific methods are as follows:

(1) Gaussian fitting is used to evaluate nonperiodic (or single-direction modulated) firing. The model function is defined as modelfunGauss1 = @(b,X) b(1) + b(2)*X + b(3)* exp [−((X(:,1) − b(4)).^2/b(5))]. The parameter structure mdl1 is obtained using fitnlm, and the goodness-of-fit is defined as Rsquared = mdl1.Rsquared.Adjusted.

(2) Cosine fitting is used to evaluate periodic firing. The model function is defined as modelfunCos = @(b,X) b(1) + b(2)* cos [2*pi/15*X + b(3)]. The parameter structure mdlcos is obtained using fitnlm, and the goodness-of-fit is defined as Rsquared = mdlcos.Rsquared.Adjusted.

Besides, Fourier transform is used to evaluate periodic firing. A Fast Fourier Transform (FFT) is applied to each head-direction tuning curve, and the power spectral density of the first 10 non-DC components is calculated: power = real(fftResult).^2 + imag(fftResult).^2. After normalization by the total power, the normalized power value at the characteristic frequency component (4 Hz, corresponding to quadruple periodicity) is used as a quantitative indicator of periodicity (Normalized Power). The analysis is implemented using MATLAB's fft function.

Data Analysis and Statistics. All statistical analyses were performed using MATLAB and GraphPad Prism 10. Welch's *t* test, paired *t* test, Mann–Whitney test, Kolmogorov–Smirnov test, and chi-square test were used as appropriate. A *P*-value of less than 0.05 was considered statistically significant.

Data, Materials, and Software Availability. Study data are included in the article and/or *SI Appendix*.

ACKNOWLEDGMENTS. This work was funded by Science Fund for Distinguished Young Scholars of Beijing (JQ23023; C.M.), the Qidong-SLS Innovation Fund (2023002029 and 2020001540; C.M.), the Space Brain Project from the Lingang Laboratory, (LG-TKN-202204-01; C.M.), the Ministry of Science and Technology of China STI 2030-Major Projects (2022ZD0206700). We gratefully thank the assistance with imaging and histology provided by the National Center for Protein Sciences at Peking University in Beijing, China. We thank Jingjing Zhang for the help of behavioral training and thank Shidan Wen and Kai Gao for their guidance on data processing.

Author affiliations: [a]State Key Laboratory of Membrane Biology, School of Life Science, Peking University, Beijing 100871, China; [b]Peking University-International Data Group/McGovern Institute for Brain Research, Peking University, Beijing 100871, China; [c]Peking-Tsinghua Center for Life Sciences, Academy for Advanced Interdisciplinary Studies, Peking University, Beijing 100871, China; [d]Peking University-Tsinghua University-National Institute of Biological Sciences Joint Graduate Program, Academy for Advanced Interdisciplinary Studies, Peking University, Beijing 100871, China; [e]Chinese Institute for Brain Research, Beijing 102206, China; and [f]Peking University Chengdu Academy for Advanced Interdisciplinary Biotechnologies, Chengdu 610213, China

1. E. I. Moser, E. Kropff, M. B. Moser, Place cells, grid cells, and the brain's spatial representation system. *Annu. Rev. Neurosci.* **31**, 69–89 (2008).
2. R. U. Muller, J. L. Kubie, The effects of changes in the environment on the spatial firing of hippocampal complex-spike cells. *J. Neurosci.* **7**, 1951–1968 (1987).
3. J. O'Keefe, D. H. Conway, Hippocampal place units in the freely moving rat: Why they fire where they fire. *Exp. Brain Res.* **31**, 573–590 (1978).
4. J. O'Keefe, A. Speakman, Single unit activity in the rat hippocampus during a spatial memory task. *Exp. Brain Res.* **68**, 1–27 (1987).

Downloaded from https://www.pnas.org by PEKING UNIVERSITY on August 3, 2026 from IP address 222.29.65.227.

5. A. Bicanski, N. Burgess, Neuronal vector coding in spatial cognition. *Nat. Rev. Neurosci.* **21**, 453–470 (2020).
6. S. D. Vann, J. P. Aggleton, E. A. Maguire, What does the retrosplenial cortex do? *Nat. Rev. Neurosci.* **10**, 792–802 (2009).
7. A. S. Alexander, R. Place, M. J. Starrett, E. R. Chrastil, D. A. Nitz, Rethinking retrosplenial cortex: Perspectives and predictions. *Neuron* **111**, 150–175 (2023).
8. N. Burgess, Spatial memory: How egocentric and allocentric combine. *Trends Cogn. Sci.* **10**, 551–557 (2006).
9. A. Bicanski, N. Burgess, A neural-level model of spatial memory and imagery. *eLife* **7**, e33752 (2018).
10. S. D. Vann, J. P. Aggleton, Extensive cytotoxic lesions of the rat retrosplenial cortex reveal consistent deficits on tasks that tax allocentric spatial memory. *Behav. Neurosci.* **116**, 85–94 (2002).
11. I. Q. Whishaw, D. J. Hines, D. G. Wallace, Dead reckoning (path integration) requires the hippocampal formation: Evidence from spontaneous exploration and spatial learning tasks in light (allothetic) and dark (idiothetic) tests. *Behav. Brain Res.* **127**, 49–69 (2001).
12. A. S. Alexander *et al.*, Egocentric boundary vector tuning of the retrosplenial cortex. *Sci. Adv.* **6**, eaaz2322 (2020).
13. P. A. LaChance, M. E. Hasselmo, Distinct codes for environment structure and symmetry in postrhinal and retrosplenial cortices. *Nat. Commun.* **15**, 8025 (2024).
14. D. Bush, C. Barry, D. Manson, N. Burgess, Using grid cells for navigation. *Neuron* **87**, 507–520 (2015).
15. J. Krupic, M. Bauza, S. Burton, J. O'Keefe, Local transformations of the hippocampal cognitive map. *Science* **359**, 1143–1146 (2018).
16. R. D. Burwell, D. G. Amaral, Cortical afferents of the perirhinal, postrhinal, and entorhinal cortices of the rat. *J. Comp. Neurol.* **398**, 179–205 (1998).
17. X. Lin *et al.*, Projection-specific circuits of retrosplenial cortex with differential contributions to spatial cognition. *Mol. Psychiatry* **30**, 2068–2084 (2025).
18. J. Sugar, M. P. Witter, Postnatal development of retrosplenial projections to the parahippocampal region of the rat. *eLife* **5**, e13925 (2016).
19. M. Gianatti *et al.*, Multiple long-range projections convey position information to the agranular retrosplenial cortex. *Cell Rep.* **42**, 113109 (2023).
20. E. Hennestad, A. Witoelar, A. R. Chambers, K. Vervaeke, Mapping vestibular and visual contributions to angular head velocity tuning in the cortex. *Cell Rep.* **37**, 110134 (2021).
21. T. Hafting, M. Fyhn, S. Molden, M. B. Moser, E. I. Moser, Microstructure of a spatial map in the entorhinal cortex. *Nature* **436**, 801–806 (2005).
22. D. Spalla, A. Treves, C. N. Boccara, Angular and linear speed cells in the parahippocampal circuits. *Nat. Commun.* **13**, 1907 (2022).
23. F. Sargolini *et al.*, Conjunctive representation of position, direction, and velocity in entorhinal cortex. *Science* **312**, 758–762 (2006).
24. T. Solstad, C. N. Boccara, E. Kropff, M. B. Moser, E. I. Moser, Representation of geometric borders in the entorhinal cortex. *Science* **322**, 1865–1868 (2008).
25. T. Wernle *et al.*, Integration of grid maps in merged environments. *Nat. Neurosci.* **21**, 92–101 (2018).
26. R. Czajkowski *et al.*, Superficially projecting principal neurons in layer V of medial entorhinal cortex in the rat receive excitatory retrosplenial input. *J. Neurosci.* **33**, 15779–15792 (2013).
27. O. W. Simonsen, R. Czajkowski, M. P. Witter, Retrosplenial and subicular inputs converge on superficially projecting layer V neurons of medial entorhinal cortex. *Brain Struct. Funct.* **227**, 2821–2837 (2022).
28. J. Sugar, M. P. Witter, N. M. van Strien, N. L. Cappaert, The retrosplenial cortex: Intrinsic connectivity and connections with the (para)hippocampal region in the rat. An interactive connectome. *Front. Neuroinform.* **5**, 7 (2011).
29. T. van Groen, J. M. Wyss, Connections of the retrosplenial granular a cortex in the rat. *J. Comp. Neurol.* **300**, 593–606 (1990).
30. T. Van Groen, J. M. Wyss, Connections of the retrosplenial granular b cortex in the rat. *J. Comp. Neurol.* **463**, 249–263 (2003).
31. M. P. Witter, T. P. Doan, B. Jacobsen, E. S. Nilssen, S. Ohara, Architecture of the entorhinal cortex a review of entorhinal anatomy in rodents with some comparative notes. *Front. Syst. Neurosci.* **11**, 46 (2017).
32. G. M. Olsen, S. Ohara, T. Iijima, M. P. Witter, Parahippocampal and retrosplenial connections of rat posterior parietal cortex. *Hippocampus* **27**, 335–358 (2017).
33. S. Keshavarzi *et al.*, Multisensory coding of angular head velocity in the retrosplenial cortex. *Neuron* **110**, 532–543.e539 (2022).
34. P. A. LaChance, J. S. Taube, Geometric determinants of the postrhinal egocentric spatial map. *Curr. Biol.* **33**, 1728–1743.e1727 (2023).
35. P. A. LaChance, J. S. Taube, A model for transforming egocentric views into goal-directed behavior. *Hippocampus* **33**, 488–504 (2023).
36. M. E. Monko, S. R. Heilbronner, Retrosplenial cortical connectivity with frontal basal ganglia networks. *J. Cogn. Neurosci.* **33**, 1096–1105 (2021).
37. K. K. Sit, M. J. Goard, Coregistration of heading to visual cues in retrosplenial cortex. *Nat. Commun.* **14**, 1992 (2023).
38. T. van Groen, J. M. Wyss, Connections of the retrosplenial dysgranular cortex in the rat. *J. Comp. Neurol.* **315**, 200–216 (1992).
39. L. M. Franco, M. J. Goard, A distributed circuit for associating environmental context with motor choice in retrosplenial cortex. *Sci. Adv.* **7**, eabf9815 (2021).
40. A. Powell *et al.*, Stable encoding of visual cues in the mouse retrosplenial cortex. *Cereb. Cortex* **30**, 4424–4437 (2020).
41. S. Trask, S. E. Pullins, N. C. Ferrara, F. J. Helmstetter, The anterior retrosplenial cortex encodes event-related information and the posterior retrosplenial cortex encodes context-related information during memory formation. *Neuropsychopharmacology* **46**, 1386–1392 (2021).
42. J. B. van Wijngaarden, S. S. Babl, H. T. Ito, Entorhinal–retrosplenial circuits for allocentric-egocentric transformation of boundary coding. *eLife* **9**, e59816 (2020).
43. G. Coughlan, J. Laczo, J. Hort, A. M. Minihane, M. Hornberger, Spatial navigation deficits–Overlooked cognitive marker for preclinical Alzheimer disease? *Nat. Rev. Neurol.* **14**, 496–506 (2018).
44. R. L. Buckner *et al.*, Molecular, structural, and functional characterization of Alzheimer's disease: Evidence for a relationship between default activity, amyloid, and memory. *J. Neurosci.* **25**, 7709–7717 (2005).
45. N. Villain *et al.*, Sequential relationships between grey matter and white matter atrophy and brain metabolic abnormalities in early Alzheimer's disease. *Brain* **133**, 3301–3314 (2010).
46. M. Pachitariu *et al.*, Suite2p: beyond 10,000 neurons with standard two-photon microscopy. bioXriv [Preprint] (2017). https://doi.org/10.1101/061507 (Accessed 11 May 2026).
47. J. Friedrich, P. Zhou, L. Paninski, Fast online deconvolution of calcium imaging data. *PLoS Comput. Biol.* **13**, e1005423 (2017).
48. A. Mathis *et al.*, Deeplabcut: Markerless pose estimation of user-defined body parts with deep learning. *Nat. Neurosci.* **21**, 1281–1289 (2018).
49. W. E. Skaggs, B. L. McNaughton, M. A. Wilson, C. A. Barnes, Theta phase precession in hippocampal neuronal populations and the compression of temporal sequences. *Hippocampus* **6**, 149–172 (1996).
50. X. Zhang *et al.*, Multiplexed representation of others in the hippocampal CA1 subfield of female mice. *Nat. Commun.* **15**, 3702 (2024).

Downloaded from https://www.pnas.org by PEKING UNIVERSITY on August 3, 2026 from IP address 222.29.65.227.